Measurements and modeling of laser-induced incandescence of soot at different heights in a flat premixed flame

Salma Bejaoui, Sébastien Batut, Eric Therssen, Nathalie Lamoureux, Pascale Desgroux, Fengshan Liu

Measurements and modeling of laser-induced incandescence of soot at different heights in a flat premixed flame

Bejaoui, Salma; Batut, Sébastien; Therssen, Eric; Lamoureux, Nathalie; Desgroux, Pascale; Liu, Fengshan

Publisher's version / Version de l'éditeur:
https://doi.org/10.1007/s00340-015-6014-3
Applied physics B: lasers and optics, 118, 3, pp. 449-469, 2015-01-28

Measurements and Modeling of Laser-Induced Incandescence of Soot at Different Heights in a Flat Premixed Flame

Salma Bejaoui[*], Sébastien Batut[*], Eric Therssen[*], Nathalie Lamoureux*, Pascale Desgroux[*]
Fengshan Liu[**1]
[*]PC2A, PhysicoChimie des Processus de Combustion et de l'Atmosphère
UMR CNRS 8522, Lille, France
[**]Black Carbon Metrology, Measurement Science and Standards
National Research Council Canada, Ottawa, Ontario, Canada K1A 0R6

[1]**Corresponding author:** Fengshan.Liu@nrc-cnrc.gc.ca

Abstract

Laser-induced incandescence (LII) experiments were conducted in a laminar flat premixed flame established with a McKenna burner at atmospheric pressure burning a rich mixture of methane, oxygen, and nitrogen with an equivalence ratio of 2.15 and with a flame stabilizer of stainless steel plate placed at 20 mm above the burner exit surface. A Nd:YAG laser operated at 1064 nm with a repetition rate of 10 Hz and a 6 ns pulse duration (FWHM) was used as the excitation source. The laser beam was shaped to achieve a reasonably uniform spatial intensity distribution. Time-resolved LII signals were measured at 610 nm (20 nm FWHM) using a PMT at different heights above the burner exit surface along the burner centerline and at different laser fluences. The soot temperature averaged over 10 ns starting at about 2 ns after the laser peak was determined through recording LII spectra with a spectrograph over the spectral range of 500 to 630 nm at different heights in the flame and at different laser fluences. Flame temperature and soot primary particle diameter and aggregate size at several flame heights were also obtained using the NO-LIF thermometry and TEM image analyses of thermophoretically sampled soot. The time-resolved LII signal and the averaged soot temperature were also modeled at different heights and different laser fluences. To achieve reasonable agreement between the modeled and experimental LII signal and soot temperature at relatively low laser-fluences it is necessary to use flame height dependent soot absorption functions. The necessity of such practice can be attributed to the continuous variation of soot thermal and/or radiative properties during the surface growth process after inception. At high laser fluences the LII models are unable to reproduce the overall shape of the normalized time-resolved LII signal profile and the averaged soot temperatures.

Key words: Flat premixed flame; Laser-induced incandescence; Time-resolved LII intensity; Soot absorption function; LIF thermometry

Introduction

Laser-induced incandescence (LII) has been developed into a powerful laser diagnostics for soot volume fraction measurement and also potentially for inferring primary soot particle diameter [1]. It has been used to measure soot volume fraction in many applications in fundamental and applied combustion, such as laminar and turbulent flames, and exhausts of automobile and aero engines. Several efforts have also been made to use low-fluence LII to infer primary particle size of non-soot nanoparticles, e.g. [2] and the references cited herein.

Although the mechanisms of soot inception and formation have been extensively investigated, they remain elusive [3]. The main steps of the overall process from gaseous hydrocarbon species to soot aggregates formed by solid carbon particles are still largely those proposed by Calcote more than three decades ago [4] with some details refined over the years [3,5]. Experimental methods leading to direct investigation of soot inception and surface growth processes remain challenging [6]. Various *in-situ* optical diagnostics providing information on soot particle size, number density, aggregate size distribution, thermal and radiative properties at different stages of soot growth are indispensable to understand soot inception, surface growth, and oxidation processes. Experimental data from optical diagnostics including primary particle and aggregate size distributions and soot volume fraction are also highly desirable for the purposes of soot model validation.

Besides being a versatile non-intrusive technique for soot volume fraction measurement, LII is also a useful tool to probe the thermal and absorption properties of soot through detecting time-resolved incandescence intensities at two or more wavelengths in the low fluence regime. This is because in this regime soot sublimation can be neglected and the physical processes of laser/soot interaction are much simpler and can be modeled with a relatively high level of confidence, though the model results are still subject to uncertainties in soot properties, such as density, specific heat, thermal accommodation coefficient and absorption function [7]. In the high laser fluence regime, where soot sublimation is significant and can no longer be neglected, however, other physical and chemical processes, such as annealing, photodesorption, and oxidation, can become important and should be taken into account [8]. Unfortunately, LII modeling in the high laser fluence regime suffers much greater uncertainties [7]. What is even

more troublesome is the fact that there is currently no consensus on what additional physical and chemical processes should be taken into account beyond the heat and mass losses associated with the thermal sublimation mechanism in modeling LII in the high laser fluence regime, let alone how to reduce the uncertainties in model parameters. Assuming there are no other physical and chemical processes in the low laser fluence regime other than laser energy absorption, soot particle internal energy change, and heat conduction with the surrounding gas molecules, the time-resolved LII signals provide rich information on the thermal and absorption/emission properties of soot, provided that the soot particle size and the local gas temperature are known. With the help of a low-fluence LII model, it is possible to infer the thermal or absorption properties of soot by matching the modeled soot temperature to the measured one. Such a low-fluence LII technique for probing the thermal and absorption properties of soot has been established by Snelling et al. to successfully derive the values of soot thermal accommodation coefficient and soot absorption function at 1064 nm in a laminar coflow ethylene diffusion flame at atmospheric pressure [9]. This approach has later been employed by other researchers to derive thermal accommodation coefficients of soot in other carrier gases [10] and in a premixed flat flame [11] and the soot absorption function $E(m)$ at different heights of flat premixed flames [11,12].

Fundamental studies of soot formation have often been conducted in laminar diffusion and premixed flames since these flames are stable and allow repeatable measurements of various quantities by laser based non-intrusive techniques and numerical simulation using detailed reaction mechanisms. Laminar axisymmetric coflow diffusion flames at normal gravity are buoyancy controlled. There are very strong gradients in the radial direction, which poses a challenge to obtain accurate measurements in such flames since it is difficult to achieve the required spatial resolution. On the other hand, flat premixed flames established with a McKenna burner in general have negligible radial gradients in the centerline region, but strong gradients along the flame height. Although it has been found that the soot thermal and radiative properties vary rapidly along the flame height in such flames, they offer a unique flame configuration to investigate the evolution of soot thermal and radiative properties at various stages of growth from incipient soot to fairly mature soot in a well characterized flame environment, since the velocity, temperature, and species concentration distributions along the flame centerline can be

computed with good accuracy under non-sooting or weakly sooting conditions [13]. Therefore, McKenna flames provide a unique flame environment to investigate soot surface growth and aggregation processes as a function of residence time through measurements of various soot properties at different height above the burner exit surface (HAB). The challenge in conducting measurements in such 'flat' premixed flames is that the flame is not always flat and can exhibit significant radial variations in temperature and soot properties [14,15], which makes the comparison between experimental data and numerical results or among experimental results from different laboratories difficult.

Several LII studies have been conducted in flat premixed flames. One of the earliest such studies was carried out by Axelsson et al. [16] who used LII for soot volume fraction and primary particle diameter measurement and laser extinction-scattering for volume equivalence particle size (sphere particle assumption). Experiments were conducted in rich flat ethylene/air premixed flames established on a McKenna burner at two equivalence rations of 2.1 and 2.3. The stabilization plate was placed at 21 mm above the burner exit surface. Measurements were made between HAB = 3 and 17 mm. A Nd:YAG laser operated at 532 nm was used as the laser source for LII. Time-resolved LII signal was detected at 400 nm (10 nm width). Although the relative prompt LII signal distribution along the flame centerline was measured for the richer flame of ϕ = 2.3, the emphasis of this study was on primary soot particle diameter determination using time-resolved LII. More recently, Stirn et al. conducted an experimental study in ethylene/air premixed flames using a McKenna burner with the stabilization plate placed at 21 mm above the burner exit surface to compare three particle sizing techniques: LII, photo-ionization mass spectrometry (PIMS), and scanning mobility particle sizing (SMPS) [17]. A revised version of the LII model of Michelsen [8] was used to infer primary particle diameter without accounting for aggregation. The equivalence ratio was varied between 1.8 and 2.6. Particle sizing was determined between 6 and 16 mm flame heights. A Nd:YAG laser operated at a wavelength of 1064 nm and 7 ns pulse duration (FWHM) was used in the LII experiments. The spatial resolution of measurement was 0.4 mm × 8 mm. LII signals were detected at 400 and 700 nm. The laser fluences were between 1.8 and 2.5 mJ/mm^2, which was quite high to induce significant soot sublimation. However, the authors claimed that there was negligible soot sublimation. They presented normalized time-resolved LII signals, but without indicating at which wavelength (400

or 700 nm). Although LII signals were detected at two wavelengths (400 and 700 nm), unfortunately, the authors did not provide any soot temperature results for the purpose of validating LII model results. Hadef et al. measured soot volume fraction and primary soot particle diameter using 2D LII and time-resolved LII, respectively, in a flat premixed ethylene-air flame established using a McKenna burner [18]. The stabilization plate was placed 21 mm above the burner exit surface. The 2D LII images were also used to indicate/monitor the uniformity of the soot volume fraction across the flame. Time-resolved LII signals were measured at HAB = 12 mm at detection wavelength of 400 nm (10 nm width) using a Nd:YAG laser operated at 1064 nm. The spatial resolution along the flame height was 0.8 mm. Soot primary particle diameter was determined by fitting the modeled normalized LII signal to the experimental one. The LII model assumed a constant thermal accommodation coefficient of 0.3 regardless HAB but temperature dependent soot density and heat capacity. Primary particle diameter measurement was conducted only at HAB = 12 mm using a laser fluence of 1.2 mJ/mm^2, but over a range of equivalence ratio between 1.9 and 2.6. The LII derived primary soot particle diameters were in very good agreement with those measured by other techniques, such as SMPS and TEM. Such good agreement is in general unexpected in this flat premixed flame. The agreement perhaps reflects the fact that at HAB = 12 mm the soot is fairly mature. Bladh et al. carried out an experimental study using low-fluence two-color LII to investigate the soot absorption coefficient $E(m)$ in the growth region of soot produced in a rich ethylene premixed flame (ϕ = 2.1) using a McKenna burner to quantitatively understand how newly formed nascent soot particles low in the flame differ in optical properties from the more mature ones at larger distances from the burner exit surface [12]. LII of soot particles was produced using a Nd:YAG laser operated at 1064 nm and the laser beam was shaped to achieve a near top-hat profile. The laser fluence was kept at 1.3 mJ/mm^2 in their study. LII signal was detected at 445 and 575 nm using PMTs. The spatial resolution at the flame height direction was 1 mm. Gas temperatures along the flame centerline were measured using coherent anti-stokes Raman spectroscopy (CARS). Primary soot particles were also measured from analysis of transmission electron microscopy (TEM) images. Assuming soot density and heat capacity remain independent of flame height, the derived $E(m)$ values from the difference between the peak soot temperature and the local gas temperature increase by more than a factor of 2 from 0.21 to 0.45 between flame

height of 7 and 17 mm. A very recent experimental study using LII and elastic light scattering (ELS) at different heights along the flat rich ethylene premixed flame conducted by the Lund group [19] confirmed the earlier finding in [12] that $E(m)$ increases with HAB. Maffi et al. conducted time-resolved two-color LII experiments in the growth region of soot in a rich ethylene/air premixed flame of $\phi = 2.3$ with a McKenna burner [11]. A Nd:YAG laser operated at 1064 nm and the laser beam was shaped to achieve a uniform and sharp-edged profile. LII signal was detected at 530 and 700 nm using PMTs. By using the measured gas temperatures along the flame centerline using a fine thermocouple and the primary particle size from their earlier study, Maffi et al. found that the values of $E(m)$ at HAB between 10 and 14 mm remain almost constant at 0.3 while the thermal accommodation coefficient increases from 0.22 to 0.34.

Although the above LII studies conducted in flat rich premixed flames reveal the capabilities of LII for soot volume fraction and primary particle diameter measurements and provide convincing evidence to demonstrate that soot absorption and/or thermal properties vary continuously in the soot growth region, they were not carried out for the purpose of establishing a comprehensive LII dataset for systematic validation of LII models. In addition, only two studies have attempted to apply the *in-situ* low-fluence LII technique to infer the soot absorption function $E(m)$ at different heights of a flat premixed flame [11,12] and only one study showed a strong variation of $E(m)$ with HAB [12]. Previous LII measurements in flat rich premixed flames were carried out in ethylene flames known to be more sooting than methane flames. The present study was motivated to provide high quality time-resolved LII signals and soot temperatures at different heights along the flame centerline and at different laser fluences and to validate LII models in the prediction of these experimental data. In this study, LII measurements were conducted in a flat premixed flame established in a commercial McKenna burner at atmospheric pressure burning a rich mixture of methane, oxygen, and nitrogen with an equivalence ratio of 2.15. The objectives of this study are threefold: (i) to report new time-resolved LII intensities and averaged soot temperature after the peak of the laser pulse at different heights above the burner exit surface and different laser fluences for known gas temperature and soot particle sizes for validation of LII models, (ii) to provide further evidence, through a comparison of the modeled and experimental results in the low fluence regime, that the thermal and/or absorption properties of soot undergo significant variations with flame height, and (iii) to validate the LII models used

in this study in terms of their ability to model both the normalized time-resolved LII signal and the soot temperature at different fluences.

Experimental Setup

Flat premixed flame

The flat premixed flame investigated in this study was stabilized on a commercial McKenna type burner at atmospheric pressure (McKenna Flat Flame Burner, Holthuis & Associates, Sebastopol, CA). This burner is made of a 60 mm diameter bronze porous sintered matrix through which a premix of methane, oxygen and nitrogen with respective volume flow rates 2.47, 2.3 and 5.17 L/min (under standard pressure and temperature) is delivered. These flow rates result in an equivalence ratio of 2.15. The flow rates of the three gases supplied to the burners were controlled by mass flow controllers. A stabilization steel plate of 60 mm diameter and 15 mm thick was placed 20 mm above the burner exit surface to stabilize the flame. A water cooling circuit is imbedded in the porous sintered matrix to prevent preheating the fresh mixture. The burner is surrounded by a co-annular porous sintered matrix which permits a flow of either air or nitrogen to shield the flame from external disturbances to improve the flame stability. In this study air was used as the shielding gas and was delivered at a flow rate of 10 L/min. The burner was mounted to a plate allowing vertical translation with a precision of 2.5 μm.

LII setup

A schematic of the LII setup is shown in Fig. 1. A Nd:YAG laser at 1064 nm with a repetition rate of 10 Hz and a 6 ns pulse duration (FWHM) was used as the excitation source of LII signals. Two detection systems perpendicular to the laser propagation direction were employed to acquire temporally and spectrally resolved LII signals, Fig. 1. For both measurements, the LII signal was collected using a set of two achromatic lenses (f_1 = 200 mm and f_2 = 600 mm) resulting a factor of 3 optical magnification. A portion of the beam section, selected with a rectangular slit, was relay imaged into the centre of the flame by means of a lens (focal length f = 200 mm) where it produced a 0.5 mm high and 2 mm wide near top-hat beam as

shown in Fig. 2. The spatial energy profile of the laser beam is also a critical parameter to provide a complete database for modeling the temporal decay of LII signals. The analysis the spatial profile of the laser beam was achieved using a beam analyzer. The spatial profiles shown in Fig. 2 are the average of 20 single-shot images from the beam profiler and are shown as 2D and 3D images with cross sections along the horizontal and vertical axis. The temporal profile of the laser beam energy is also an important parameter in LII modeling and was also obtained in this study, as shown in Fig. 3, using a photodiode (Thorlabs DET 210 with a rise time of 1 ns).

For time-resolved LII measurements, the radiation passes through a slit of 1.5 mm in height and 15 mm in z direction in front of the PMT, Fig. 1, allowing the selection of the entire volume irradiated by the laser. A band pass filter at 610 nm (20 nm FWHM) is placed in front of the PMT (Philips XP 2237 B) powered by a Hamamatsu power supply (C7169). Two hundred LII temporal profiles were averaged on a digital oscilloscope (Lecroy technology, 500 MHz bandwidth, 2.5 GS/s sampling rate) triggered by a signal from a photodiode (Hamamatsu S 1722-02) whose rise time is 2 ns and its spectral response range is between 200 nm and 1000 nm. An average signal without laser irradiance was subtracted in order to offset flame luminosity and electronic interferences caused by the laser power supply.

For soot temperature measurements around the end of the laser pulse at different heights in the flame and at different laser fluences, LII spectra were recorded with a spectrograph formed with a monochromator (Action 300 I) with a 150-g/mm 300-nm blazed grating and a gated ICCD camera (Princeton PiMAX). The exposure time was fixed at 10 ns starting at 8 ns after the first photons of the laser, i.e., at about 26 ns in Fig. 3. The calibration of the detection system was performed using an optical sphere (SphereOptics CSTM-LR-6-M), which is in very good approximation to a blackbody radiator with a temperature of 3220 K. The optical setup and detection angle were the same for the calibration and detection of the soot emission. The spectrograph wavelength calibration was performed using spectral lines from mercury (Oriel 6035) emission lamp. All the spectra used for soot temperature determination were subtracted from the background flame emission.

Assuming primary soot particles are in the Rayleigh regime in the visible spectral range, the calibrated spectral LII intensity can be expressed as

$$LII(\lambda,T) = 48E(m)\frac{\pi^2 hc^2}{\lambda^6}\left[\exp(\frac{hc}{\lambda k_B T}) - 1\right]^{-1} f_v \quad (1)$$

where λ is wavelength, T is soot temperature, f_v is soot volume fraction, h, c, and k_B are the Planck constant, the speed of light, and the Boltzmann constant, respectively. By using the Wien approximation Eq. (1) can be written as

$$\ln(\frac{LII(\lambda,T)\lambda^6}{E(m)}) = -B\frac{1}{\lambda} + \ln(A) \quad (2)$$

Where $A = 48\pi^2 hc^2 f_v$ and $B = hc/(k_B T)$. Therefore, the soot temperature can be determined from the slope of the curve of $\ln(LII(\lambda,T)\lambda^6/E(m))$ vs. $1/\lambda$. The slope of this curve was calculated over the spectral range of 500 and 630 nm. In this study $E(m)$ was assumed to be independent of wavelength and also independent of flame heights in the estimate of soot temperature.

Gas temperature by NO-LIF thermometry

For LII modeling and to make the experimental LII results useful for LII model validation, it is important to know the local gas temperature. For this purpose, the gas temperature was measured using NO-LIF thermometry.

NO detection by laser-induced fluorescence (LIF) is a laser diagnostic allowing *in-situ* determination of flame temperature. The technique mostly relies on the excitation of several rotational transitions of NO molecule scanned using a tunable laser source. It was shown to be well suited for stationary flames from low pressure to high pressure as previously detailed in [20,21,22]. Furthermore capabilities of multi-line NO-LIF thermometry has also been demonstrated to measure the temperature of sooting flames by exciting transitions from the A-X(0,0) of NO around 226 nm or from the *D-X*(0,1) around 193 nm [23]. Each excitation scheme requires its own collection strategy to prevent spectral interferences from flame emission, soot incandescence, PAH LIF [24] or O_2 LIF [23]. In order to improve the signal to noise ratio measurements a small quantity of NO is seeded in the reactive flow. The quantity is small enough so that the temperature of the flame can be considered unchanged in presence of seeding.

When the rotational lines are well isolated one from each other, the temperature is readily obtained by plotting the LIF intensities as function of the rotational energies of the excited transitions (Boltzmann plot) [23,25]; otherwise, the temperature can be determined from the best fit between the experimental spectrum and a library of simulated spectrum calculated on a large range of temperatures. Synthetic spectra are calculated using a simple steady-state two-level model with excitation in the linear regime. They take into account experimental parameters such as baseline, experimental line shape, bandwidth, pressure and temperature. In our work we use LIFBASE [26] to generate our library of synthetic spectra. Experimental spectra were corrected for laser spectral irradiance variation. Independence of the fluorescence quantum yield with rotational energy for NO molecule was considered consistently with literature [20,21,24]. 1000 ppm of NO was seeded into the flame to compensate its consumption which occurs mainly in the flame-front. This quantity was found sufficient to guarantee a good signal to noise ratio even in the burnt gases of the sooting flame, a condition which was not reachable by LIF thermometry on native OH radical. This NO level is within a range previously shown as not perturbing the flame temperature (0.2 to 1% in Ref. 21 and 300-2000 ppm in Ref. 24). In addition, the reduced NO-seeding allows to neglect both the rotational energy dependent absorption of the laser energy across the flame and trapping. The comparison of flame temperatures obtained either by OH LIF thermometry or by NO-LIF thermometry using the Boltzmann plot performed in a rich non sooting low-pressure methane flame where OH thermometry is possible [25] was extended to the NO-thermometry method based on calculated spectra. A good agreement was found between these methods.

In the following temperatures were determined using the multi-line NO-LIF thermometry method associated with synthetic spectra analysis. The laser system consists of a frequency-doubled Nd:YAG Continuum laser pumping a dye laser. Wavelengths around 225 nm were obtained by mixing the residual infrared radiation of the YAG laser with the doubling of the fundamental dye radiation. The 6-ns-duration pulse had bandwidths around 1 cm^{-1}. The laser energy fluctuations were monitored by a postflame photodiode located after the burner enclosure. The laser beam was introduced unfocused parallel to the burner surface and shaped using a horizontal slit of 1.5 mm in front of the burner. The LIF signal was collected at f/4 by a two-lens system and focused on the entrance slit of a 0.275-m monochromator. The entrance slit, adjusted

to width 250 μm and height 10 mm, was parallel to the laser axis, and the output slit was adjustable to provide a 8-nm bandpass adapted to collect the A-X(0,2) the fluorescence band under investigation. Under these conditions, measurements were found free from possible background from LII, PAH LIF and flame emission. The fluorescence signals were collected with a 1.5-ns rise-time Philips XP2020Q photomultiplier tube. The fluorescence and laser intensity signals were stored by a digital scope (LECROY 9354A, 8-bit, 500-MHz bandwidth, 1 GS/s sampling rate). The excitation LIF spectrum was recorded by scanning the wavelength from 225.43 to 225.75 nm with a scan rate of the fundamental dye wavelength of 0.5 pm/s and by averaging the LIF signals over seven laser pulses. Rotational levels comprised between 10 and 44 were probed in the A-X(0,0) band. The baseline was determined for each spectrum around 225.44 nm and subtracted all along the recorded spectrum. A post-treatment consisting of a Savitzky–Golay smoothing filter with a moving window of 25 points was applied. Temperature was determined from the least mean square between the experimental and the simulated spectrum. An example of fit is shown in Fig. 4.

Soot sampling/TEM image analysis

Knowledge of primary soot particle diameter and aggregate size distributions is very important for LII model validation. For this purpose, soot was sampled thermophoretically at selected flame heights along the flame centerline. The sampling device consists of a pneumatic piston with a stroke distance of 10 cm. At flame heights above 10 mm it was found that a single insertion of the sampling probe into the flame with a residence time of 640 ms is sufficient to obtain an adequate coverage of soot particles on the grid. At a lower flame height of HAB = 9 mm, however, multiple insertions of the sampling probe to the flame was found necessary to get enough soot particles on the grid for image analysis. Images of the sampled soot were generated using transmission electron microscope (TEM) for analysis of primary soot particle diameter and aggregate size distributions. At even lower flame heights (< 9 mm), attempts to collect soot particles suitable for TEM image analysis were not successful. At heights below 9 mm there exists only newly formed 'young' soot particles, which are liquid-like with relatively low carbon content [19,27].

Image J software was used in the TEM image analysis. Primary soot particle distributions were obtained manually by carefully identifying individual primary particles from TEM images. Soot aggregate size distributions were derived from the ratio of the projected area of aggregate to that of a primary particle of averaged diameter using the correlation of Köylü et al. [28].

LII Model

In this study modeling of the LII signal and soot temperature was conducted using two LII models: (i) a base model and (ii) an extended model. The base LII model (hereafter Model 1) incorporates only the commonly accepted heat and mass transfer processes, namely laser energy absorption, soot particle internal energy change, heat conduction, and thermal sublimation. Thermal radiation from soot particles contributes negligibly to particle heat loss during LII at atmospheric pressure. Both models take into account the effect of particle aggregation on heat conduction using the heat transfer equivalence sphere model developed by Liu et al. [29]. The base LII model, Model 1, has been discussed in detail in several previous publications [7,29], only a brief description is provided here.

Model 1: the base model

Model 1 is formulated in terms of energy and mass conservation equations written for a soot aggregate consisting of N_p identical primary particles

$$\frac{1}{6}\pi d_p{}^3 N_p \rho_s c_s \frac{dT}{dt} = C_{abs}{}^{agg} F_0 q(t) - q_c + \frac{\Delta H_v}{M_v}\frac{dM}{dt} \tag{3}$$

$$\frac{dM}{dt} = \frac{1}{2} N_p \rho_s \pi d_p{}^2 \frac{dd_p}{dt} = -\pi d_p{}^2 N_p \beta_0 p_v \sqrt{\frac{M_v}{2\pi R_u T}} \tag{4}$$

where ρ_s and c_s are the density and specific heat of soot, t is time, N_p the aggregate size (the number of primary particles) $C_{abs}{}^{agg}$ is the absorption cross-section of the aggregate, F_0 is the laser fluence, $q(t)$ is the laser power temporal profile corresponding to per unit laser fluence, q_c is aggregate heat loss rate due to conduction. The last term in Eq. (3) represents aggregate sublimation heat loss rate with M being the aggregate total mass, M_v the mean molecular weight of the sublimated species, and ΔH_v the heat of sublimation. In Eq. (4) p_v is the sublimation

pressure, R_u is the universal gas constant (8.3145 J/mol K), and β_0 the effective sublimation coefficient. Soot aggregate conduction heat loss, q_c, was calculated using the expressions given in [29]. It is implicitly assumed in Eqs. (3) and (4) that any potential temperature non-uniformity among primary particles within an aggregate was neglected. Other assumptions in the development of aggregate LII model were discussed in [29]. It is also worth pointing out that the effect of aggregation on soot sublimation, the last term on the right hand side of Eq. (3), was neglected due to lack of better knowledge.

Effect of aggregation on the aggregate absorption cross-section $C_{abs}{}^{agg}$ has been investigated in two recent studies [30,31], where it was found that the Rayleigh-Debye-Gans theory for fractal aggregate (RDG-FA) can cause significant error in aggregate absorption cross-section when the primary particle diameter and the degree of aggregation are fairly large. The simple RDG-FA approximation was used in this study based on the considerations that both the primary soot particle diameters and aggregate sizes in the flat premixed flame are fairly small. The aggregate absorption cross-section can then be expressed as

$$C_{abs}{}^{agg} = N_p \frac{\pi^2 d_p{}^3 E(m)}{\lambda} \tag{5}$$

Most of the thermal properties of soot described in several previous studies [7,9,32], such as density, specific heat, thermal conductivity of the surrounding gas, mean molecular weight of the sublimated species, sublimation pressure, and sublimation enthalpy, were also used in this study. Based on the consideration that soot properties vary in the growth region in McKenna premixed flames [11,12], the soot absorption coefficient $E(m)$ was treated as an adjustable model parameter. Although the thermal accommodation coefficient α was found to increase with HAB in the growth region of a rich ethylene flame by Maffi et al. [11], a fixed at 0.37 was used in this study. The effective sublimation coefficient β_0 was also treated as an adjustable model constant.

Model 2: the extended model

To improve the performance of Model 1 at high laser fluences where heat and mass loss by sublimation is important, Model 1 was extended to the effects of C_2 photodesorption based on the LII models of Michelsen [7,8]. In addition, the more detailed sublimation sub-model of Michelsen [7,8] was also employed in the extended model. However, soot oxidation was neglected based on the consideration that it is unimportant for the time scales of LII processes and the soot density was considered as temperature independent (same as Model 1). Although annealing was implemented in the original LII model of Michelsen and shown to be important [8], it was neglected in a more recent LII model of Michelsen [7] without explanation. For this reason annealing was also neglected in the present study. A detailed description of the sublimation sub-model, with photodesorption included, used in the extended LII model is available in [7,8]. Only a brief summary of the model is given below.

In the extended LII model the sublimation sub-model was reformulated following the work of Michelsen [7,8]. The desorption of carbon clusters from soot particles is attributed to both the thermal mechanism (the normal sublimation) and the non-thermal mechanism (photodesorption). The total energy loss rate due to sublimation from a soot aggregate can be written as [7], assuming aggregation does not affect the sublimation process,

$$Q_{sub} = N_p \sum_{j=1}^{5} \frac{1}{W_j} \left(\frac{dm_p}{dt} \right)_j \left(\frac{\Delta H_j (P_{sat}{}^{C_j} - P_{\lambda n}) + \Delta H_{\lambda n} P_{\lambda n}}{P_{sat}{}^{C_j}} \right) \tag{6}$$

where subscript j refers to each desorbed species (j = 1, 2, …,5), ΔH_j is the enthalpy of formation of carbon vapor species C_j and is listed in Table III in [8]. $P_{sat}{}^{Cj}$ and $P_{\lambda n}$ are the saturation partial pressure of C_j and the effective partial pressure due to photodesorption of C_2, respectively. Quantity $\Delta H_{\lambda n}$ is the energy required to photodesorb C_2.

The rate of primary particle mass loss due to sublimation is written as

$$\left(\frac{dm_p}{dt} \right)_j = \frac{-\pi d_p{}^2 W_j U_j \beta_j B_j}{R_p T} \quad , j = 1, 2, \ldots, 5 \tag{7}$$

where U_j and β_j are the average velocity of C_j moving away from the particle surface and the mass accommodation coefficient of C_j (given as α_j in Table III in [8]). R_p is the universal gas constant in effective pressure units (82.058 atm cm^3/mol K). U_j is calculated as

$$U_j = \sqrt{\frac{R_m T}{2\pi W_j}} \tag{8}$$

where R_m is the universal gas constant in effective mass units (8.3145×10^7 g cm^2/mol K s^2). Parameter B_j in Eq. (7) denotes a pressure factor representing the influence of diffusive and convective mass transfer during sublimation. Following Michelsen [8], parameter B_j is calculated as follows

$$B_j = \frac{2D_{eff} P_{sat}^{C_j}}{d_p \beta_j U_j + 2D_{eff}} \quad \text{, when } P_{sat}^{Cj}/P_0 < 3\times10^{-3} \tag{9}$$

$$B_j = P_{sat}^{C_j} - P_{surf}^{C_j} \quad \text{, when } P_{sat}^{Cj}/P_0 > 3\times10^{-3} \tag{10}$$

where P_0 is the ambient pressure and P_{surf}^{Cj} is the partial pressure of C_j at the particle surface. D_{eff} is the total effective diffusion constant.

In this sublimation model both the thermal sublimation and non-thermal sublimation (photodesorption) processes contribute to the instantaneous partial pressure of sublimated species. The partial pressure of C_j contributed by the thermal sublimation of particles is determined by P_{equil}^{Cj}, which is the thermal equilibrium partial pressure of C_j is calculated using the Clausius-Clapeyron equation as

$$P_{equil}^{C_j} = P_{ref} \exp\left(\frac{\Delta S_j}{R_u} - \frac{\Delta H_j}{RT}\right) \tag{11}$$

where P_{ref} is the reference pressure (1 atm) and R_u is the universal gas constant (8.3145 J/mol K). The entropies of formation of carbon clusters (ΔS_j) are also provided in Table III in [8]. It is noted that three different forms of the universal gas constant are used in Eqs. 7, 8, and 11 for convenience of numerical implementation. Care should be taken for the units of the involved

quantities in these equations. When the effective pressure from the nonthermal photodesorption mechanism exceeds the thermal equilibrium partial pressure, thermal desorption will cease. When this happens, the effective pressure is equal to that due to photodesorption of carbon C_2.

The saturation partial pressure of C_j at the particle surface is determined as follows [8]

$$P_{sat}^{C_j} = P_{equil}^{C_j}, \quad \text{if} \quad P_{equil}^{C_j} > P_{\lambda n} \tag{12}$$

$$P_{sat}^{C_j} = P_{\lambda n}, \quad \text{if} \quad P_{\lambda n} > P_{equil}^{C_j} \tag{13}$$

The effective pressure contributed by the non-thermal photodesorption is expressed as

$$P_{\lambda n} = \frac{k_P T k_{\lambda n}}{\pi d_p^{\,2} \beta_j U_j} \tag{14}$$

where k_P is the Boltzmann constant in effective pressure units (1.3626×10^{-22} atm cm^3/K). The rate constants (1/s) is given as [7]

$$k_{\lambda n} = \frac{\lambda}{nhc} \frac{\pi d_p^{\,3} \sigma_{\lambda n} N_{ss}}{6} \frac{B_{\lambda n}^{\,n}}{q_n} \times \left\{ 1 - \exp\left[-\left(\frac{q(t) F_0}{B_{\lambda n}} \right)^n \right] \right\} \tag{15}$$

where N_{ss} is the density of carbon atoms on the surface of particles ($N_{ss} = 2.8\times10^{15}$ cm^{-2}), $\sigma_{\lambda n}$ is an empirical constant for multiphoton absorption cross section for photodesorption of C_2. Michelsen [7] assigned a value of 1.9×10^{-10} cm^{2n-1}J^{1-n}. $B_{\lambda n}$ is another empirical constant for saturation coefficient for multiphoton absorption and was assigned a value of 0.5 J/cm^2 [7]. The nondimensional exponent n was used to estimate the dependence of the nonthermal photodesorption rate on the laser fluence (or the number of 532-nm photons absorbed to photodesorbed C_2) and was set to 2 [7,8]. Quantity q_n is a normalization constant for the integrated laser temporal profile raised to the nth power, i.e.,

$$q_n = \int_0^\infty q_0^{\,n}(t) dt \tag{16}$$

where q_0(t) is the nondimensional reduced laser temporal profile which has a peak value of unity.

In the absence of annealing the total effective diffusion constant D_{eff} in Eq. (9) can be approximated as [8]

$$D_{eff} = D_{eff}^{C_3} \tag{17}$$

The effective diffusion coefficient of carbon species C_j can be calculated using the following expression [8]

$$D_{eff}^{C_j} = \frac{3fk_pT}{4\sigma_j P_0}\sqrt{\frac{R_m}{\pi W_j}}\frac{(T + A_0/A_1)^2 - (T_0 + A_0/A_1)^2}{\sqrt{T}(T + 3A_0/A_1) - \sqrt{T_0}(T_0 + 3A_0/A_1)} \tag{18}$$

where f is the Eucken factor, $f = (9\gamma\text{-}5)/4$, with γ being the specific heat ratio of carbon clusters, P_0 and T_0 are the ambient pressure (in atm) and the initial particle temperature (the same as the local gas temperature), respectively. Parameters σ_j is the mean molecular cross section of species C_j and is given in Table III in [8]. Parameters A_0 and A_1 can be found in Table IV in [8].

Finally the partial pressure of C_j at the particle surface (in atm) is calculated as [8]

$$P_{surf}^{C_j} = \frac{P_0}{\eta}\left[1 - \frac{2D_{eff}}{d_p\beta_j U_j}J(z)\right] \tag{19}$$

where

$$z = \frac{d_p\beta_j U_j}{2D_{eff}}\exp\left[\frac{d_p\beta_j U_j}{2D_{eff}}\left(1 - \frac{\eta P_{sat}^{C_j}}{P_0}\right)\right] \tag{20}$$

$$J(z) = z \text{ , if } z \le 3\times10^{-3} \tag{21}$$

$$J(z) = 0.92267z^{0.98535}\text{, if } 3\times10^{-3} < z < 0.05$$

$$\begin{aligned} J(z) = {} & 5.815\times10^{-1} + 3.496\times10^{-1}(\ln z) \\ & +6.516\times10^{-2}(\ln z)^2 + 1.667\times10^{-3}(\ln z)^3 \\ & -6.031\times10^{-4}(\ln z)^4 - 4.161\times10^{-5}(\ln z)^5 \end{aligned} \quad \text{, if } 0.05 < z < 300$$

$$J(z) = -1.189 + 9.187\times10^{-1}(\ln z), \quad \text{if } z > 300$$

and

$$\eta = \frac{P_0 + \sum_{i=1}^{5} P_{sat}{}^{C_j}}{P_{sat}{}^{C_j}} \tag{22}$$

The heat conduction sub-model remains the same as in Model 1. The energy conservation equation in Model 2 remains the same as that in Model 1 given in Eq. (3) with the exception that the sublimation heat loss term, i.e., the last time on the right hand side of Eq. (3), is now replaced by the term given in Eq. (6). The mass conservation equation in Model 2 is now expressed as

$$\frac{dM}{dt} = \frac{1}{2} N_p \rho_s \pi d_p{}^2 \frac{dd_p}{dt} = N_p \sum_{j=1}^{5} \left(\frac{dm_p}{dt} \right)_j \tag{23}$$

where the primary particle mass loss rates are given in Eq. (7).

Accounting for polydispersity of primary soot particle and aggregate sizes

The energy and mass conservation equations of an LII model are solved for specified values of N_p and d_p at a given gas temperature and laser fluence. The effect of polydispersity in N_p and d_p on LII modelling is accounted for by solving the model governing equations for a range of values of N_p and d_p, depending on the problem at hand, and then the time-resolved effective soot temperature and LII signal are obtained by integration over the aggregate size and primary particle diameter distributions. In this practice it is assumed that primary soot particle diameters are identical within a given aggregate, but are allowed to vary from aggregate to aggregate. In this study the model equations were solved for aggregate size between 1 and 50 and the primary particle diameter between 2 and 35 nm for given initial temperature and laser fluence.

To simulate the time-resolved LII signal detected at 610 nm and the average effective soot temperature near the end of the laser pulse in the experiments described in the last section the contributions from each aggregate must be integrated over the aggregate size and primary

particle diameter distributions. Following a previous study [29], both the aggregate size and primary particle diameter distributions are assumed to be log-normal, i.e.,

$$p(N_p) = \frac{1}{N_p \sqrt{2\pi}\ln\sigma_{N,g}} \exp\left[-\left(\frac{\ln(N_p/N_g)}{\sqrt{2}\ln\sigma_{N,g}}\right)^2\right] \tag{24}$$

$$p(d_p) = \frac{1}{d_p \sqrt{2\pi}\ln\sigma_{d,g}} \exp\left[-\left(\frac{\ln(d_p/d_g)}{\sqrt{2}\ln\sigma_{d,g}}\right)^2\right] \tag{25}$$

where N_g and $\sigma_{N,g}$ in Eq. (24) are the two parameters of the distribution function and represent respectively the geometric mean aggregate size and the geometric standard deviation. Similarly, parameters d_g and $\sigma_{d,g}$ in Eq. (25) are the geometric mean primary particle diameter and the geometric standard deviation for the distribution of d_p. The total LII signal at a detection wavelength λ can then be expressed as

$$S_\lambda = \Theta \int_1^\infty \int_0^\infty p(N_p)p(d_p)N_p \frac{2\pi c^2 h}{\lambda^5}\left[\exp\left(\frac{hc}{\lambda k_B T(d_p, N_p)}\right) - 1\right]^{-1} \frac{\pi^2 {d_p}^3 E(m)}{\lambda} \mathrm{d}d_p \mathrm{d}N_p \tag{26}$$

where Θ is a constant and is dependent on detection system setup and the flame height. Let's define an average effective temperature T_e which would represent the temperature of soot particles as deduced by the temporal integration of the LII signal over 10 ns and is defined as follows:

$$\frac{\int_{\tau_1}^{\tau_2} S_{\lambda_1} dt}{\int_{\tau_1}^{\tau_2} S_{\lambda_2} dt} = \frac{E(m_1)}{\lambda_1^{\,6}} \frac{{\lambda_2}^6}{E(m_2)} \frac{\exp(hc/k_B\lambda_2 T_e) - 1}{\exp(hc/k_B\lambda_1 T_e) - 1} \tag{27}$$

where τ_1 and τ_2 are the beginning and end of the ICCD exposure ($\tau_2 = \tau_1 + 10$ ns), λ_1 and λ_2 are 500 and 630 nm, respectively. After making the Wien approximation, i.e, $\exp(hc/k_B\lambda T) \gg 1$, which is valid under the present conditions, substitution of Eq. (26) into Eq. (27) leads to

$$T_e = \frac{hc}{k_B}\left(\frac{1}{\lambda_2} - \frac{1}{\lambda_1}\right) / \ln\left(\frac{\int_{\tau_1}^{\tau_2}\int_1^\infty\int_0^\infty p(N_p)N_p p(d_p){d_p}^3 \exp(-hc/k_B\lambda_1 T)\mathrm{d}d_p\mathrm{d}N_p dt}{\int_{\tau_1}^{\tau_2}\int_1^\infty\int_0^\infty p(N_p)N_p p(d_p){d_p}^3 \exp(-hc/k_B\lambda_2 T)\mathrm{d}d_p\mathrm{d}N_p dt}\right) \tag{28}$$

It is noticed that the soot temperature in the integrals of Eq. (28) is dependent on time t, aggregate size N_p, and the primary particle diameter d_p. A series of solutions for a range of prescribed primary soot particle diameter and aggregate size is first obtained by solving the energy and mass conservation equations as discussed earlier. These solutions serve as a database for evaluation of the integrations in Eq. (28) to obtain the average effective temperature T_e.

Results and Discussion

The measured gas temperatures

The measured gas temperatures by NO-LIF thermometry at HAB between 6 and 16 mm are shown in Fig. 5. They result from an average of two series. The accuracy is estimated to around ± 100 K. It is interesting to note that this figure also shows the calculated gas temperature distributions along the flame centerline by the CHEMKIN code for three different inlet temperatures (600 to 800 K) and a plate temperature of 900 K. The plate temperature of 900 K was measured by a thermocouple. The combustion chemistry was modeled using the GRI-Mech 3.0 mechanism [33], which was optimized for methane combustion. Under the experimental conditions of this study the flat premixed flame is stabilized just above the porous metal burner surface (less than 1 mm). Therefore, there is significant heat transfer from the reaction zone to the porous metal burner material, which in turn preheats the fresh fuel mixture. As such, there is uncertainty in the inlet mixture temperature. The assumed inlet temperatures between 600 and 800 K in the numerical simulation are estimated based on the measurements of Migliorini [34] using a thermocouple in an ethylene/air premixed flame of ϕ = 2.34 and those of Tsurikov et al. [35] in an ethylene/air premixed flame of ϕ = 2.30 using CARS. In addition to the uncertainty in the inlet mixture temperature, the predicted temperature distributions also suffer uncertainties associated with the absence of PAH and soot formation in numerical simulation and of radiative transfer. Nevertheless, the agreement between the measured and the calculated gas temperatures between HAB = 7 and 16 mm can be regarded as reasonably good. This finding is important since it indicates that the modeled temperature profile can be used with some confidence when the measured gas temperature profile is not available. The measured gas temperatures over this

range of HAB are also in fairly good agreement with those measured by Bladh et al. [12] using CARS in an ethylene/air flat premised flame of ϕ = 2.1. The measured gas temperatures were used in LII modeling.

Soot primary particle diameter and aggregate size distributions

The primary soot particle diameter distributions at four heights, HAB = 9, 11, 13, and 15 mm, along the flame centerline were obtained by identifying manually many individual primary particles from TEM images. The results are shown in Fig. 6. Also plotted in Fig. 6 are the lognormal fits to each distribution. The size of each aggregate on TEM images is estimated from its projected area, which can be obtained with image processing software, such as Image J. The aggregate size can be related to its two-dimensional projected area through the following correlation

$$N_p = k_a (A_a / A_p)^{\alpha} \tag{29}$$

where k_a is a proportional constant of order 1, α is an empirical projected area exponent, A_a and A_p are the projected areas of the aggregate and a primary particle of average diameter, respectively. The present TEM image analysis for N_p was conducted using k_a = 1.16 and α = 1.1 following the study of Köylü et al. [28].

The lognormal distribution parameters fit for the TEM image derived d_p and N_p distributions at HAB = 9, 11, 13 and 15 mm are summarized in Table 1. Although the lognormal distribution parameters for d_p and N_p at HAB = 7 and 8 mm are also shown in Table 1, they were not obtained from TEM image analysis but estimated based on the trends of the lognormal parameters over the range of 9 to 15 mm above the burner exit.

The d_p and N_p distributions at HAB = 7 and 8 mm are required to derive $E(m)$ at these heights. Although d_g increases slightly from 9.5 nm at HAB = 9 mm to 10.3 nm at HAB = 15 mm, the corresponding increases in N_p is more significant. In addition, the standard deviations of both d_p and N_p between HAB = 9 and 15 mm remain almost constant at 1.15. These results suggest that the increase in primary soot particle size nearly ceases while soot particles undergo

strong aggregation over this range of flame heights, in agreement with the findings of Bladh et al. [12] obtained in a flat premixed ethylene/air flame of ϕ = 2.1. The mean primary soot particle diameters at HAB = 9, 11, 13, and 15 mm, calculated as $\bar{d}_p = d_g \exp[0.5\ln(\sigma_{dg})^{0.5}]$, are 11.5, 11.9, 12, and 12.4 nm, respectively. These mean primary soot particle diameters are very close to, but somewhat smaller than those obtained by Bladh et al. [12] over the same range of HAB in the flat premixed ethylene/air flame of ϕ = 2.1, as expected from the relative sooting tendency of methane and ethylene.

Measured averaged soot temperatures

The measured averaged soot temperatures over 10 ns shortly after the peak of the laser pulse (between 26 and 36 ns shown in Fig. 3) at different flame heights and different laser fluences are shown in Fig. 7. Two observations can be readily made from this figure. First, at a given fluence below about 1.5 mJ/mm^2 the soot temperature reaches a higher value at a higher height, though the local flame temperature decreases with height as shown in Fig. 5. This is an indication of the variation of soot thermal and/or radiative properties as soot evolves from 'young' to more 'mature' soot, which will be discussed further later. Secondly, at high fluences above 4 mJ/mm^2, where significant sublimation and possibly other physical and chemical process take place, the soot temperatures at HAB below 10 mm behave differently from those at above HAB = 10 mm. At HAB < 10 mm, the soot temperature continues to increase with fluence. At HAB > 10 mm, soot temperatures are independent of heights and increase at a slower rate with fluence. What is more interesting is that the soot temperatures at HAB > 10 mm are lower than those at lower heights at fluences higher than 4 mJ/mm^2. It is attempting to explain the lower soot temperature at higher heights at these very high fluences as follows. The more mature soot particles at HAB > 10 mm absorb more laser energy and reach sublimation temperatures earlier than those at HAB < 10 mm and therefore soot temperatures during the fixed 10 ns period are lower due to sublimation cooling. Unfortunately, the numerical results shown below do not support this explanation.

Variation of E(m) along the flame centerline

Assuming the density and heat capacity of soot particles remain flame height independent one can derive the variation of soot absorption function $E(m)$ at 1064 nm with flame height using the soot temperatures at low fluences, the local gas temperature, and the energy balance equation of LII (without sublimation contributions) [9,12]. In this study the value of $E(m)$ was derived by matching the calculated average soot temperature over the 10 ns period to the measured one in the range of about 3300 to 3500 K based on the following two considerations. First, lower measured soot temperatures below 3300 K are likely less accurate due to reduced signal-to-noise ratios. Secondly, soot temperatures higher than 3500 K can cause non-negligible sublimation and affect the derived value of $E(m)$.

The $E(m)$ values at 1064 nm between HAB = 7 and 15 mm derived from this study are compared with those of Bladh [12] from an ethylene/air flat premised flame of $\phi = 2.1$ in Fig. 8. $E(m)$ increases with increasing HAB in both studies. The values of $E(m)$ derived in the present study are higher than those of Bladh et al. at HAB lower than about 9 mm, but are lower at higher flame heights, i.e., the present derived E(m) does not vary with HAB as strongly as that in the study of Bladh et al. [12]. The increase of $E(m)$ found in ethylene premixed flames is also found in the rich methane premixed flame studied here (and probably in any mixture). The amplitude of the variation is probably linked to the "rate of maturity" of the soot. The present study confirms that $E(m)$ changes as soot particles undergo structural and/or compositional changes during their surface growth and coagulation. Nevertheless, the results shown in Fig. 8 suggest that soot properties, such as density, heat capacity, or the absorption function $E(m)$, vary significantly over the growth region of the flame and caution should be taken when assuming soot has the same properties over an entire flame in optical diagnostics of soot.

Time-resolved LII signal and averaged soot temperature: Model 1

It is noted that the time-resolved LII signal was detected at 610 nm, which is within the spectral range considered for the soot temperature determination. The measured and calculated LII signal at HAB = 9 mm, where soot particles are quite liquid-like, by Model 1 using a high value of effective sublimation coefficient of $\beta_0 = 0.77$ are compared in Fig. 9. The calculated LII

signals are normalized at temporal peak using the values of experiment and modeling at F_0 = 1.064 mJ/mm^2. At fluences below 1.064 mJ/mm^2, Model 1 reproduces the signal peaks, but predicts a slower signal decay, Fig. 9(a). At higher fluences, however, Model 1 underpredicts the signal peak, especially at fluences above 1.473 mJ/mm^2 and overpredicts the signal decay, Fig. 9(a). At fluences above 2 mJ/mm^2, the calculated LII signals are about a factor of 2 to 3 lower than the measured ones, Fig. 9(b). In addition, the modelled LII signals display much weaker dependence on the laser fluence than the measured ones.

A comparison of the measured and modeled time-resolved LII signals at a higher flame height of HAB = 12 mm, where soot particles get more 'mature', and different laser fluences is given in Fig. 10. It is noted that the normalization at HAB = 12 mm was done to match the experimental peak at F_0 = 1.376 mJ/mm^2. Overall, similar observations as those made in Fig. 9 can be made. However, it is noticed that the underprediction of LII signals at fluences above 2 mJ/mm^2, Fig. 10(b), is not as severe as that at HAB = 9 mm shown in Fig. 9(b), suggesting that the LII model parameters are more relevant to the soot particles at HAB = 12 mm than at lower flame heights. It is evident from the high fluence results shown in Fig. 10(b) that the modelled LII signal peaks increasingly earlier with increasing laser fluence, while the measured peak appears more or less at the same time for fluences between 1.864 and 4.091 mJ/mm^2 (it appears only slightly earlier). The experimental LII signals at F_0 = 4.091 mJ/mm^2 are actually lower than those at F_0 = 3.209 mJ/mm^2 after the peak of the signal, which can be attributed to the rapid mass loss of soot particles at such high fluences. It is interesting to observe that Model 1 is capable of capturing this phenomenon, Fig. 10(b).

The measured and modeled averaged soot temperature over 10 ns after the laser peak at different laser fluences and different flame heights are compared in Fig. 11. The modeled soot temperatures are in fairly good agreement with measured ones at relatively low fluences below about 2 mJ/mm^2 at HAB = 7, 8, and 9 mm and below about 2.5 mJ/mm^2 at higher flame heights, which is somewhat expected due to use of HAB dependent $E(m)$ in the modeling. Overall, Model 1 using β_0 = 0.77 underpredicts soot temperatures at high fluences, especially at HAB below 10 mm, Fig. 11(a). At HAB above 10 mm, Fig. 11(b), both the measured and modeled temperatures display very small dependence on HAB and the discrepancies between the measured and

modeled values are also smaller. The lower calculated soot temperatures is at least partially responsible for the lower calculated LII signals at higher fluences shown in Figs. 9 and 10.

Results shown in Figs. 9 to 11 suggest that the LII model overestimates the heat and mass loss associated with sublimation at high laser fluences. To investigate how Model 1 performs with suppressed sublimation the Model 1 results shown in Fig. 9 to 11 were repeated for a much smaller effective sublimation coefficient of $\beta_0 = 0.1$. Model 1 results obtained using $\beta_0 = 0.1$ are compared to the experimental results in Figs. 12, 13, and 14 for time-resolved LII signal at HAB = 9, 12 mm, and averaged soot temperature, respectively. It is evident by a direct comparison between Figs. 9 and 12 and Figs. 10 and 13 that the agreement between the modeled and measured time-resolved LII signal is significantly improved at fluences above about 1.4 mJ/mm^2 at both HAB = 9 and 12 mm, especially at HAB = 12 mm, Fig. 13. However, the modeled soot temperatures are substantially higher than the measured ones, especially at HAB above 10 mm, Fig. 14(b). An examination of the results shown in Figs. 11 and 14 implies that an effective sublimation coefficient around $\beta_0 = 0.5$ might result in fairly good agreement between the modeled and the measured soot temperatures over the fluences and flame heights considered. However, such better agreement in soot temperature is gained at the cost of worse agreement in the time-resolved LII signal. Therefore, it is important to take into account both time-resolved signal and soot temperature in the optimization of LII model parameters.

Time-resolved LII signal and averaged soot temperature: Model 2

In the calculations of Model 2 the mass accommodation coefficients were chosen as 0.2, 0.2, 0.03, 1.0×10^{-4}, and 1.0×10^{-4} for C_1 to C_5 based on the studies of Michelsen [8] and Pflieger et al. [36]. Other parameters for soot sublimation in Model 2 were all taken from Michelsen [7,8]. Numerical difficulties were encountered when the laser fluence was higher than about 3.2 mJ/mm^2. Therefore, no numerical results were obtained at fluences higher than 3.2 mJ/mm^2.

The modeled LII signals by Model 2 are compared with the measured ones at HAB = 9 and 12 mm in Figs. 15 and 16. At HAB = 9 mm the modeled peak LII signals at fluences up to 1.686 mJ/mm^2 are in very good agreement with the measured values, Fig. 15(a). The modeled

signal decay is also in reasonably good agreement with the measured one. At higher fluences, the modeled results display increasingly larger discrepancy with the measured ones. Even so, Model 2 still performs better than Model 1 as long as the time-resolved LII signal at HAB = 9 mm is concerned, Figs. 9, 12, and 15. At a higher flame height of HAB = 12 mm the modeled peak LII signals are in very good agreement with the measured ones for all the fluences considered up to 3.209 mJ/mm^2, albeit Model 2 predicted a faster rise in the signal at fluences above 2.343 mJ/mm^2 and a faster LII signal decay at fluences above 1.864 mJ/mm^2. Once again Model 2 outperforms Model 1 in terms of the time-resolved LII signal at HAB = 12 mm, Figs. 10, 13, and 16.

The modeled average soot temperatures over 10 ns after the laser peak by Model 2 at HAB = 7, 8, 9 and 11 mm are compared with the measured ones in Fig. 17. The modeled soot temperatures by Model 2 increase more rapidly with fluence than the measured ones and those calculated by Model 1 with $\beta_0 = 0.1$, Fig. 14. It is therefore clear that the better calculated time-resolved LII signals by Model 2 compared with the measured ones than those by Model 1 is companied with worse agreement between the calculated and measured soot temperatures. The even higher soot temperatures calculated by Model 2 than Model 1 using $\beta_0 = 0.1$ are not surprising if one realizes that C_3 is the dominant sublimated carbon species and a smaller mass accommodation coefficient of $\beta_3 = 0.03$, which is equivalent to the effective sublimation coefficient in Model 1, was used in Model 2. It can be conjectured from the results shown in Figs. 12 to 17 that inclusion of photodesorption of C_2 does not affect the results of Model 2 significantly.

Conclusions

Laser-induced incandescence measurements were carried out in the soot growth region in a rich flat CH_4 premixed flame at different heights above the burner exit surface and different laser fluences. Time-resolved LII signal and averaged soot temperature over 10 ns after laser peak were measured at different flame heights and over a wide range of laser fluences. To support numerical modeling of LII, gas temperature and soot primary particle diameter and level of aggregation were also measured using NO-LIF thermometry and TEM image analysis. The

comprehensive experimental results of the present study are valuable for validation of LII models. This study made the first attempt to model the measured average soot temperatures after the peak of the peak of laser pulse and time-resolved LII signal in the soot growth region of the rich flat CH_4 flame for the purpose of validating two LII models, which differ in the treatment of soot sublimation. A general remark can be made is that it is very challenging to model the heat and mass transfer processes during LII in the soot growth region of rich flat premixed flames since soot particles undergo continuously varying thermal and optical properties from inception to more 'mature' state. The following conclusions can be drawn based on the results of this study.

1. Soot particles undergo significant increase in their ability to absorb laser energy with the value of $E(m)$ increasing from about 0.22 at HAB = 7 mm to about 0.37 at HAB = 15 mm under the present experimental conditions. This finding is in qualitative agreement with the earlier study of Bladh et al. [12].

2. The commonly used effective sublimation coefficient of 0.77 or greater in the soot sublimation sub-model is too high to predict reasonable average soot temperatures after the laser pulse peak and time-resolved LII signal in the high fluence regime under conditions of this study. A smaller value of the effective sublimation coefficient improves the agreement between the modeled soot temperatures and the measured values. However, satisfactory agreement in both the modeled time-resolved LII signal and the averaged soot temperature at different flame heights and different laser fluences cannot be achieved by adjusting the value of the effective sublimation coefficient.

3. The revised LII model using a more detailed description of the soot sublimation process improves the agreement between the modeled time-resolved LII signal and the measured one, but worsens the agreement between the modeled soot temperature and the measured one.

4. The photodesorption of C_2 does not seem to play a significant role relative to the thermal mechanism in soot sublimation. More research efforts are required to improve the LII model at high laser fluences.

5. It should be emphasized that it is important to take into account of both time-resolved LII signal and soot temperature over a wide range of laser fluences to systematically validate an LII model or optimize some model parameters.

Acknowledgements

The work conducted at PC2A was supported by the Air Quality Program of CPER-IRENI (Institut de Recherche en ENvironnement Industriel) and the Labex CaPPA through the Programme d'Investissement d'Avenir (ANR-11-LABX-005-01). FL would like to acknowledge the financial support by NRCan PERD AFTER Project C23.006.

References

1. Schulz, C., Kock, B.F., Hofmann, Michelsen, H., Will, S., Bougie, B., Suntz, R., Smallwood, G., Laser-induced incandescence: recent trends and current questions, Appl. Phys. B 83 (2006) 333-354.

2. Cignoli, F., Bellomunno, C., Maffi, S., Zizak, G., Laser-induced incandescence of titania nanoparticles synthesized in a flame, Appl. Phys. B 96 (2009) 593-599.

3. Wang, H., Formation of nascent soot and other condensed-phase materials in flames, proc. Combust. Inst. 22 (2011) 41-67.

4. Calcote, H.F., Mechanisms of soot nucleation in flames – A critical review, Combust. Flame 42 (1981) 215-242.

5. Bockhorn, H., Soot Formation in Combustion: Mechanisms and Models, Springer-Verlag, Berlin, 1994.

6. Desgroux, P., Mercier X., Thomson, K.A., Study of the formation of soot and its precursors in flames using optical diagnostics, Proc. Combust. Inst. 34 (2013) 1713-1738.

7. Michelsen, H.A., Liu, F., Kock, B.F., Bladh, H., et al., Modeling laser-induced incandescence of soot: a summary and comparison of LII models, Appl. Phys. B 87 (2007) 503-521.

8. Michelsen, H.A., Understanding and predicting the temporal response of laser-induced incandescence from carbonaceous particles, J. Chem. Phys. 118 (2003) 7012-7045.

9. D. R. Snelling, F. Liu, G. J. Smallwood, and Ö. L. Gülder, Determination of the soot absorption function and thermal accommodation coefficient using low-fluence LII in a laminar coflow ethylene diffusion flame, Combust. Flame, 136: 180-190, 2004.

10. K.J. Daun, G.J. Smallwood, F. Liu, Investigation of thermal accommodation coefficients in time-resolved laser-induced incandescence, ASME J. Heat Transfer, 130: 121201, 2008.

11. S. Maffi, S. De Iuliis, F. Cignoli, and G. Zizak, Investigation on thermal accommodation coefficient and soot absorption function with two-color Tire-LII technique in rich premixed flames, Appl. Phys. B, 104: 357-366, 2011.

12. H. Bladh, J. Johnsson, N.-E. Olofsson, A. Bohlin, P.-E. Bengtsson, Optical soot characterization using two-color laser-induced incandescence (2C-LII) in the soot growth region of a premixed flat flame, Proc. Combust. Inst., 33: 641-648, 2011.

13. Abid, A.D., Camacho, J., Sheen, D.A., Wang, H., Quantitative measurement of soot particle size distribution in premixed flames – The burner-stabilized stagnation flame approach, Combust. Flame 156 (2009) 1862-1870.

14. F. Migliorini, S. De Iuliis, F. Cignoli, and G. Zizak, How "flat" is the rich premixed flame produced by your McKenna burner? Combust. Flame, 153: 384-393, 2008.

15. N. E. Olofsson, H. Bladh, A. Bohlin, J. Johnsson, and P.-E. Bengtsson, Are sooting premixed porous-plug burner flames one-dimensional? A laser-based experimental investigation, Combust. Sci. Tech., 185 (2013) 293-309.

16. Axelsson, B., Collin, R., Bengtsson, P.-E., Laser-induced incandescence for soot particle size measurements in premixed flat flames, Applied Optics, 39:3683-3690, 2000.

17. R. Stirn, T. G. Baquet, S. Kanjarkar, W. Meier, K. P. Geigle, H. H. Grotheer, C. Wahl, and M. Aigner, Comparison of particle size measurements with laser-induced incandescence, mass spectroscopy, and scanning mobility particle sizing in a laminar premixed ethylene/air flame, Combust. Sci. Tech., 181:329-349, 2009.

18. R. Hadef, K. P. Geigle, W. Meier, M. Aigner, Soot characterization with laser-induced incandescence applied to a laminar premixed ethylene-air flame, Int. J. Thermal Sci., 49: 1457-1467, 2010.

19. N.-E. Olofsson, J. Johnsson, H. Bladh, P.-E. Bengtsson, Soot sublimation studies in a premixed flat flame using laser-induced incandescence (LII) and elastic light scattering (ELS), Appl. Phys. B, 112: 333-342, 2013.

20. M. Tamura, J. Luque, J.E. Harrington, P.A. Berg, G.P. Smith, J.B. Jeffries, D.R. Crosley, Laser-induced fluorescence of seeded nitric oxide as a flame thermometer, Appl. Phys. B 66: 503–510, 1998.

21. A.T. Hartlieb, B. Atakan, K. Kohse-Höinghaus, Temperature measurement in fuel-rich non-sooting low-pressure hydrocarbon flames, Appl. Phys. B 70: 435–445, 2000.

22. A.O. Vyrodov, J. Heinze, M. Dillmann, U.E. Meier, W. Stricker, Laser-induced fluorescence thermometry and concentration measurements on NO A-X (0-0) transitions in the exhaust gas of high pressure CH_4/air flames, Appl. Phys. B 61: 409-414, 1995.

23. K. Hayashida, K. Amagai, M. Arai, LIF thermometry in sooty flames using NO $D^2\Sigma^+ \leftarrow X^2\Pi(0,1)$ and OH $A^2\Sigma^+ \leftarrow X^2\Pi(3,0)$ bands, Energy 30: 497-508, 2005.

24. W.G. Bessler, C. Schulz, Quantitative multi-line NO-LIF temperature imaging, Appl. Phys. B 78 : 519-533, 2004.

25. N. Lamoureux, P. Desgroux, A. El Bakali, J.F. Pauwels, Experimental and numerical study of the role of NCN in prompt-NO formation in low-pressure CH_4-O_2-N_2 and C_2H_2-O_2-N_2 flames, Comb. Flame 157: 1929–1941, 2010.

26. J. Luque, D.R. Crosley, LIFBASE: Database and Spectral Simulation (Version 1.5), SRI International Report MP 99-009, 1999.

27. S. De Iuliis, S. Maffi, F. Cignoli, G. Zizak, Three-angle scattering/extinction versus TEM measurements on soot in premixed ethylene/air flame, Appl. Phys. B, 102: 891-903, 2011.

28. Ü.Ö. Köylü, G.M. Faeth, T.L. Farias, M.G. Carvalho, Fractal and projected structure properties of soot aggregates, Combust. Flame, 100: 621-633, 1995.

29. F. Liu, M. Yang, F. A. Hill, D. R. Snelling, G. J. Smallwood, Influence of polydisperse distributions of both primary particle and aggregate size on soot temperature in low-fluence LII, Applied Physics B 83, 383-395 (2006).

30. F. Liu, G.J. Smallwood, Effect of aggregation on the absorption cross-section of fractal soot aggregates and its impact on LII modelling, JQSRT 111 (2010) 302-308.

31. F. Liu, G.J. Smallwood, The effect of particle aggregation on the absorption and emission properties of mono- and polydisperse soot aggregates, Applied Physics B (2011) 104:343-355.

32. G.J. Smallwood, D.R. Snelling, F. Liu, and Ö. L. Gülder, Clouds over soot evaporation: errors in modeling laser-induced incandescence of soot, ASME J. Heat Transfer (2001) 123:814-818.

33. G.P. Smith, D.M. Golden, M. Frenklach, N.W. Moriarty, B. Eiteneer, M. Goldenberg, C.T. Bowman, R.K. Hanson, S. Song, W.C. Gardiner Jr., V.V. Lissianski, and Z. Qin, http://www.me.berkeley.edu/gri_mech/.

34. F. Migliorini, Study of combustion process of hydrogen-hydrocarbon mixtures. Ph.D thesis, Politecnico di Milano, Italy (2008).

35. M.S. Tsurikov, K.P. Geigle, V. Krüger, Y. Schneider-Kühnle, W. Stricker, R. Lückerath, R. Hadef, M. Aigner, Laser-based investigation of soot formation in laminar premixed flames at atmospheric and elevated pressures, Combust. Sci. Tech., 177: 1835-1862, 2005.

36. R. Pflieger, M. Sheindlin, J.Y. Colle, Advances in the mass spectrometry study of the laser vaporization of graphite, J. Appl. Phys. 104, 054902/1-054902/6, 2008.

Table 1 Primary soot particle diameter and aggregate size distributions obtained from TEM image analysis at different heights along the flame centerline.

HAB, mm	d_g, nm	σ_{dg}	N_g	σ_{Ng}
7*	8.5	1.15	1.2	1.05
8*	9.0	1.15	1.5	1.05
9	9.5	1.15	2	1.1
11	9.8	1.17	4	1.15
13	10.0	1.15	6	1.15
15	10.3	1.15	8	1.15

*The distributions of d_p and N_p at HAB = 7 and 8 mm are estimated using the trend over the HAB from 9 to 15 mm.

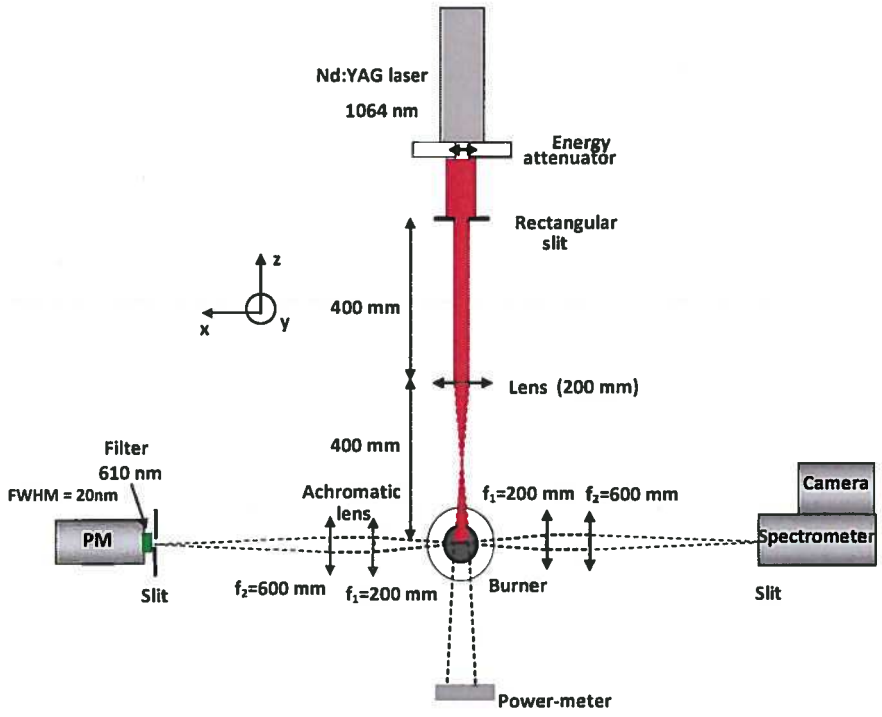

Fig. 1. Experimental apparatus for temporally and spectrally resolved LII measurements.

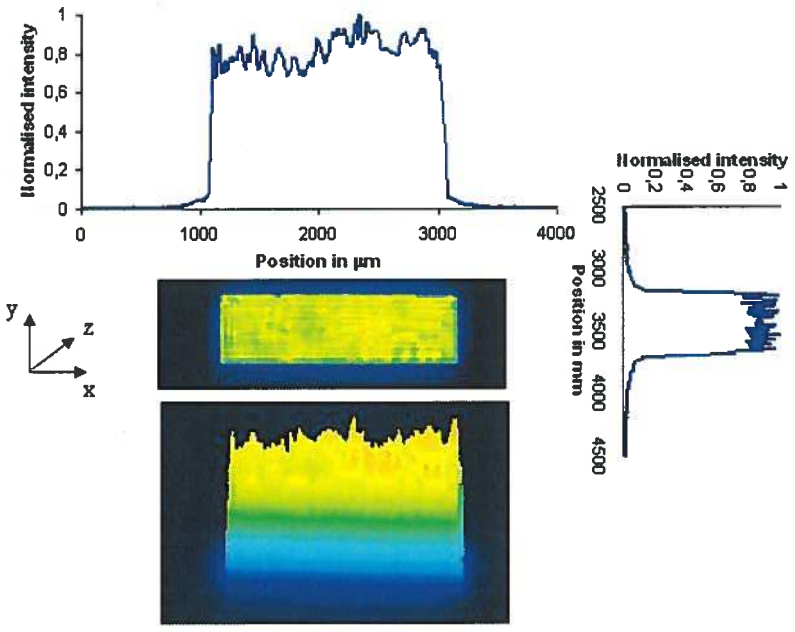

Fig. 2 The spatial profiles of the laser beam energy.

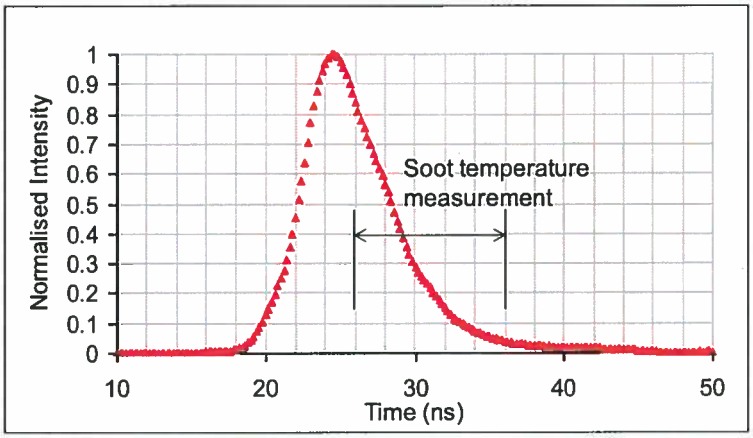

Fig. 3 The temporal profile of the laser beam and the period for soot temperature measurement.

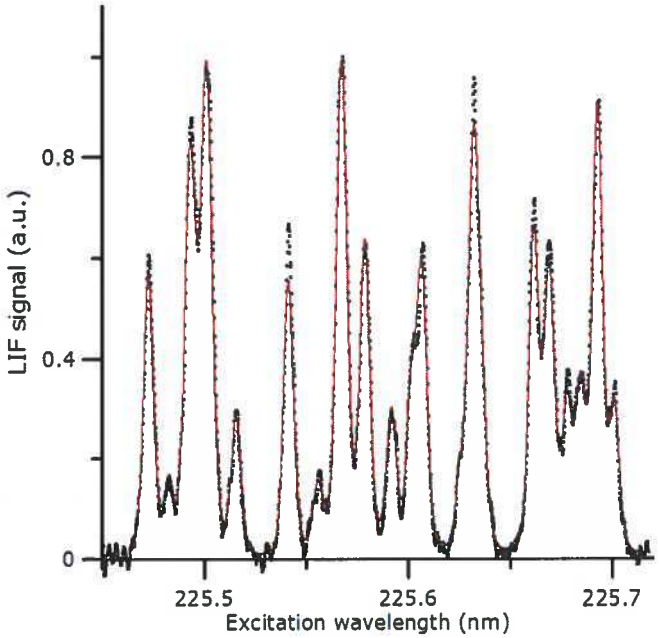

Fig. 4 Experimental (symbols) and fitted simulated (line) excitation spectra of NO A-X(0,0) band for HAB = 6 mm and T = 1920 K.

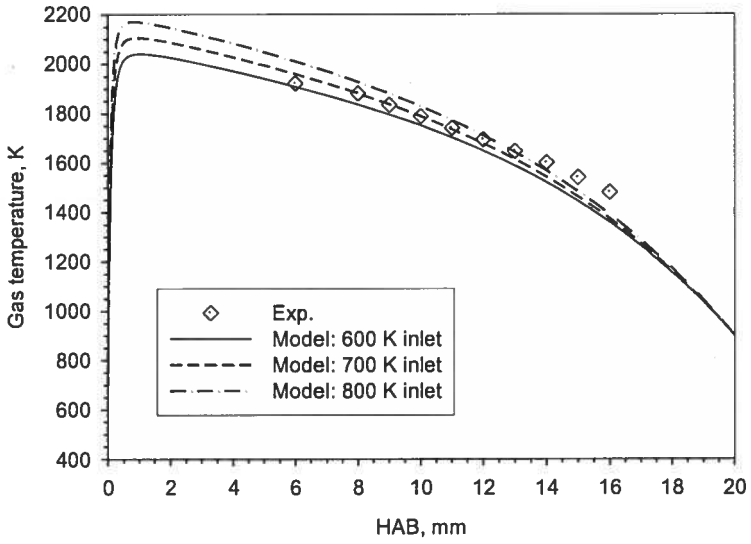

Fig. 5 Comparison of the calculated gas temperature distributions along the flame centerline for different inlet mixture temperatures and the measured temperatures by NO-LIF pyrometry.

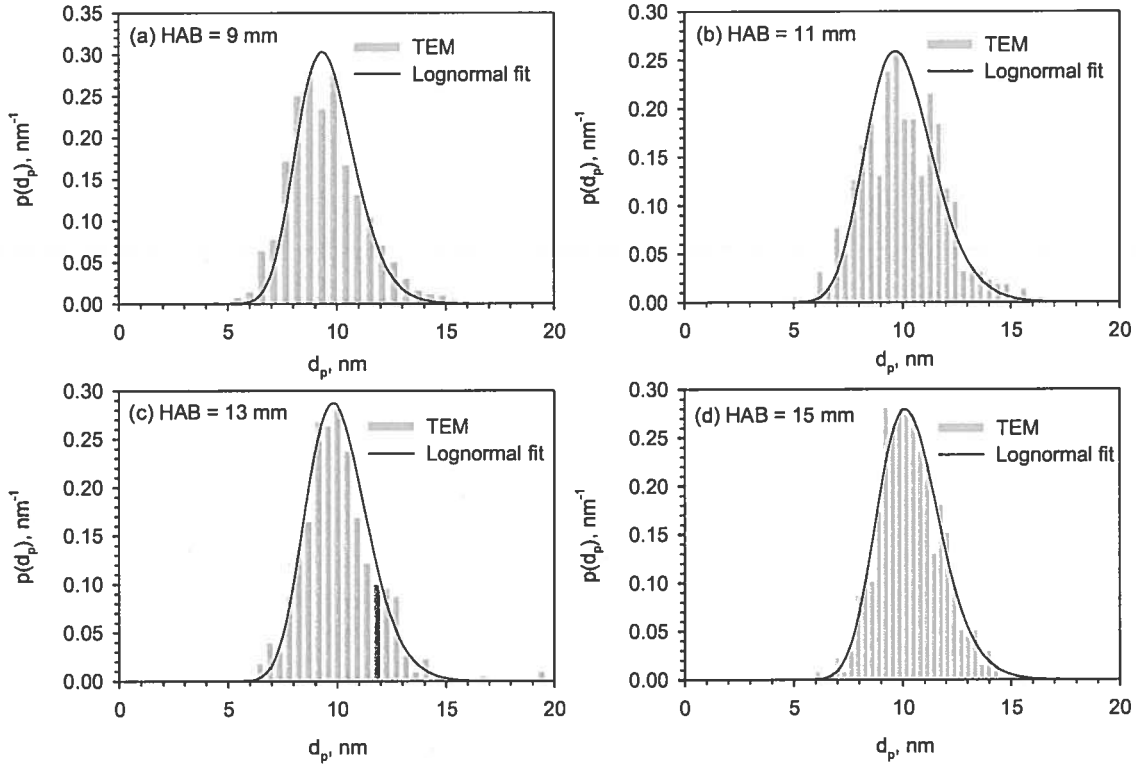

Fig. 6 Primary soot particle diameter distributions at HAB = 9, 11, 13, and 15 mm.

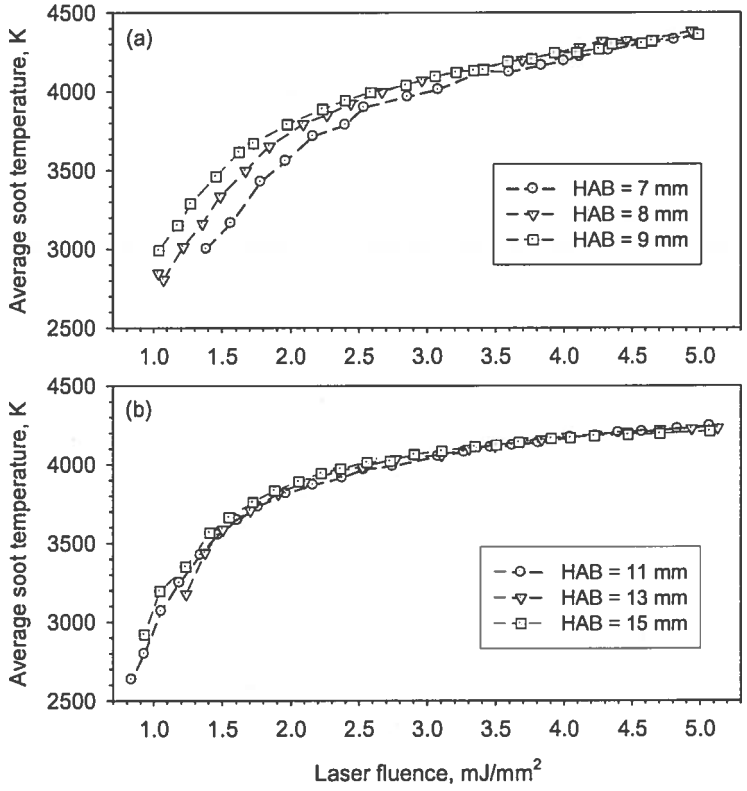

Fig. 7 The measured average soot temperature over 10 ns shortly after the peak of the laser pulse at different flame heights and different laser fluences.

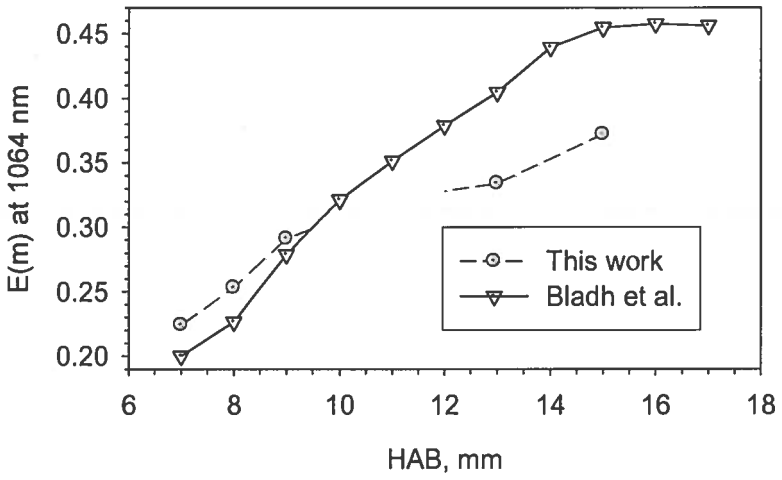

Fig. 8 The soot absorption function E(m) at 1064 nm derived from the measured soot temperature at low laser fluences.

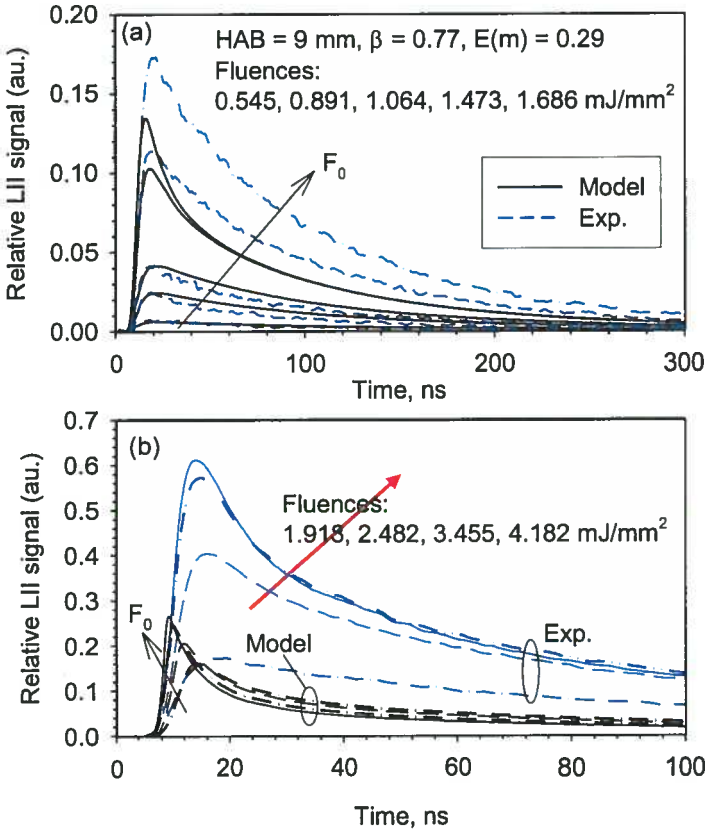

Fig. 9 Comparison of the measured and calculated time-resolved LII signals at different laser fluences: Model 1, HAB = 9 mm, $\beta_0 = 0.77$ (normalized at $F_0 = 1.064$ mJ/mm^2).

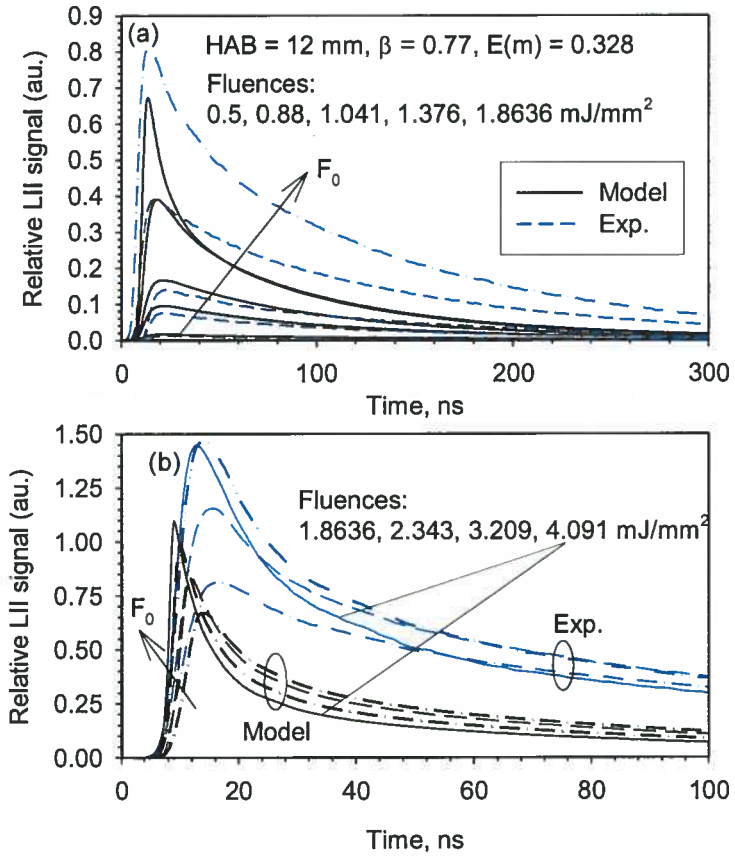

Fig. 10 Comparison of the measured and calculated time-resolved LII signals at different laser fluences: Model 1, HAB = 12 mm, $\beta_0 = 0.77$ (normalized at $F_0 = 1.376$ mJ/mm^2).

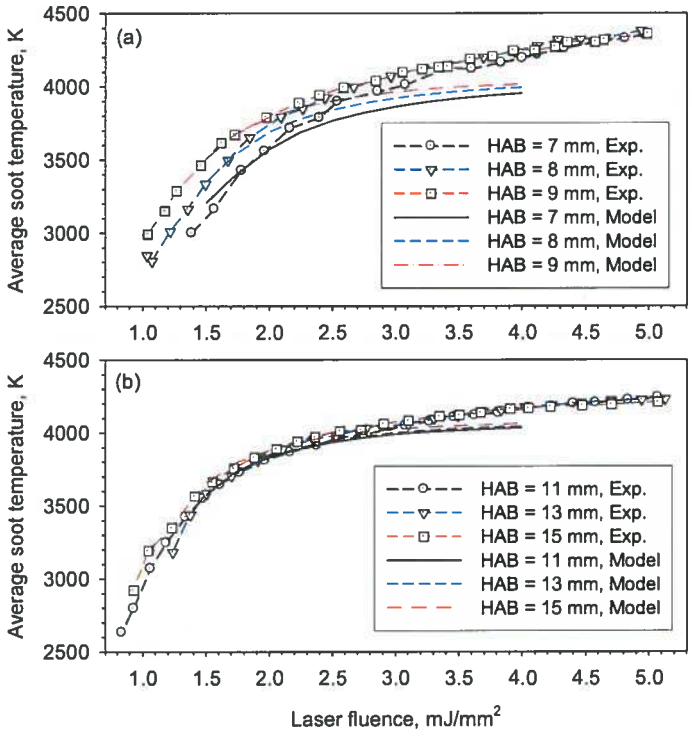

Fig. 11 Comparison of measured and modeled averaged soot temperature over 10 ns after the laser peak: Model 1, $\beta_0 = 0.77$.

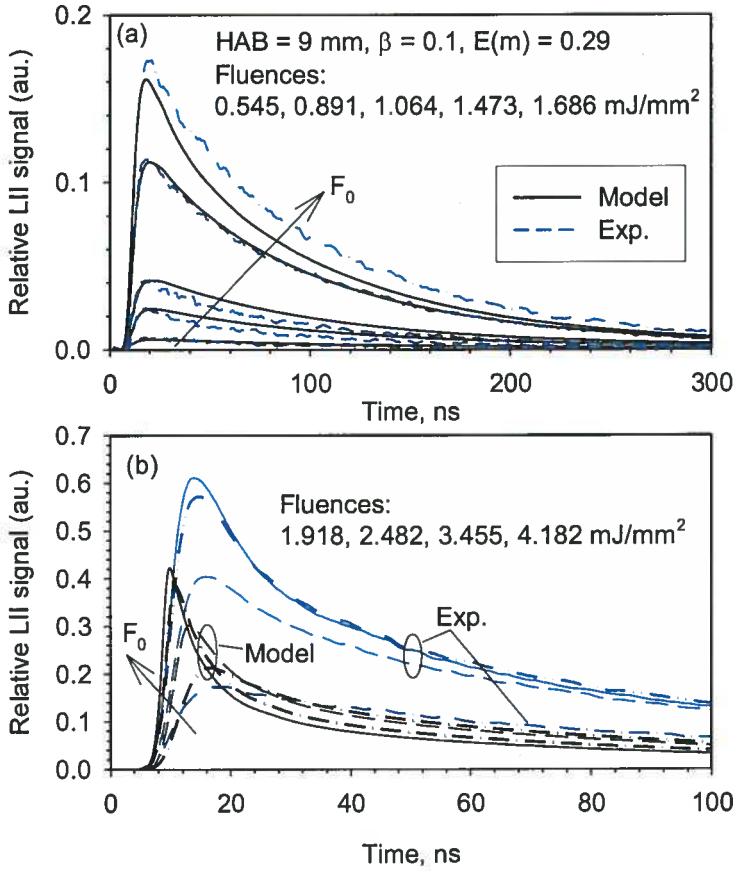

Fig. 12 Comparison of the measured and calculated time-resolved LII signals at different laser fluences: Model 1, HAB = 9 mm, $\beta_0 = 0.1$ (normalized at $F_0 = 1.064$ mJ/mm^2).

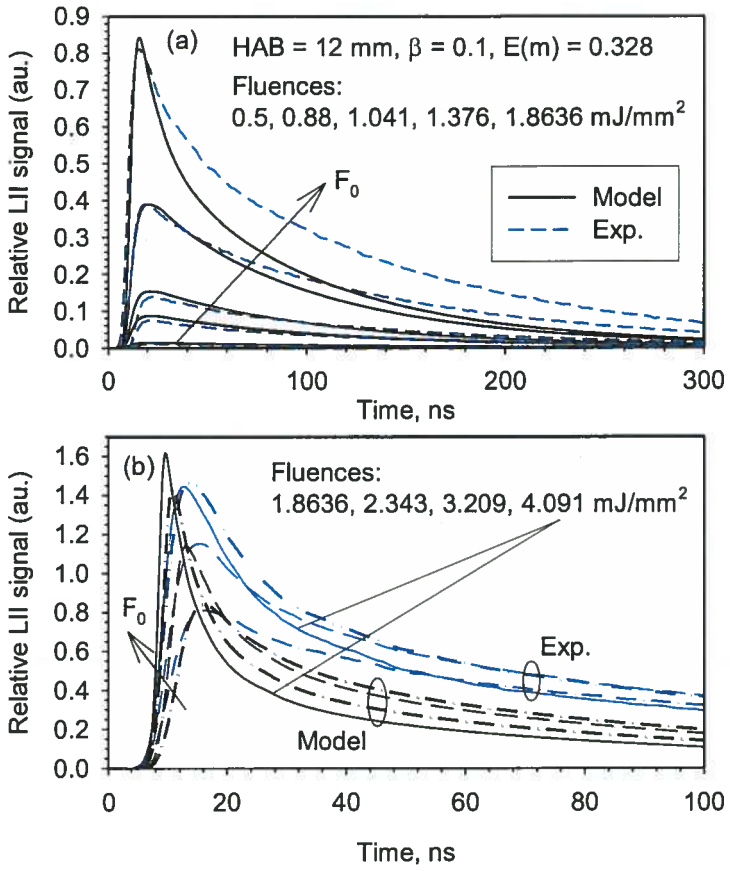

Fig. 13 Comparison of the measured and calculated time-resolved LII signals at different laser fluences: Model 1, HAB = 12 mm, $\beta_0 = 0.1$ (normalized at $F_0 = 1.376$ mJ/mm^2).

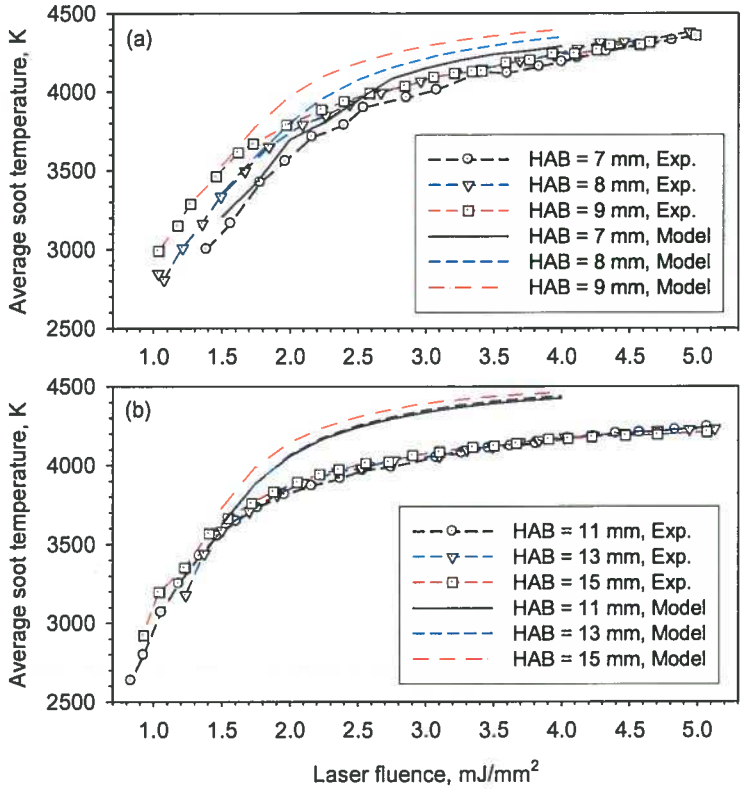

Fig. 14 Comparison of measured and modeled averaged soot temperature over 10 ns after the laser peak: Model 1, $\beta_0 = 0.1$.

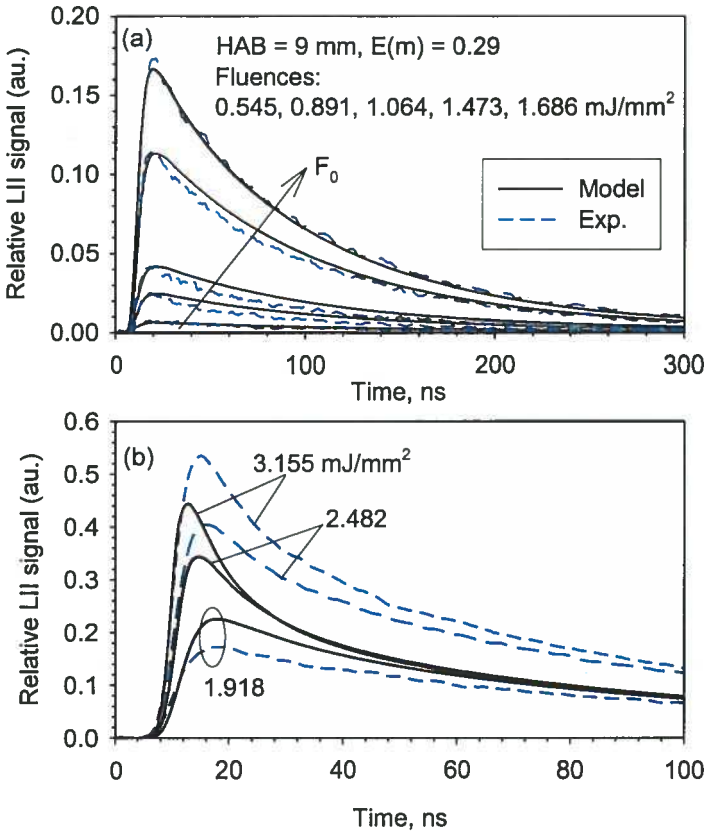

Fig. 15 Comparison of the measured and calculated time-resolved LII signals at different laser fluences: Model 2 at HAB = 9 mm (normalized at F_0 = 1.064 mJ/mm^2).

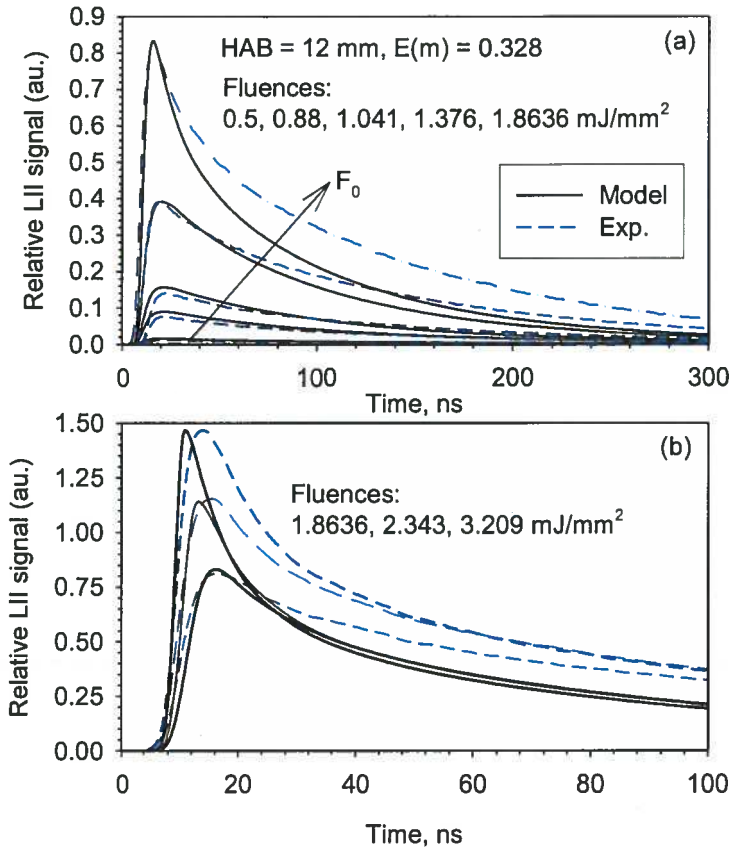

Fig. 16 Comparison of the measured and calculated time-resolved LII signals at different laser fluences: Model 2 at HAB = 12 mm (normalized at F_0 = 1.376 mJ/mm^2).

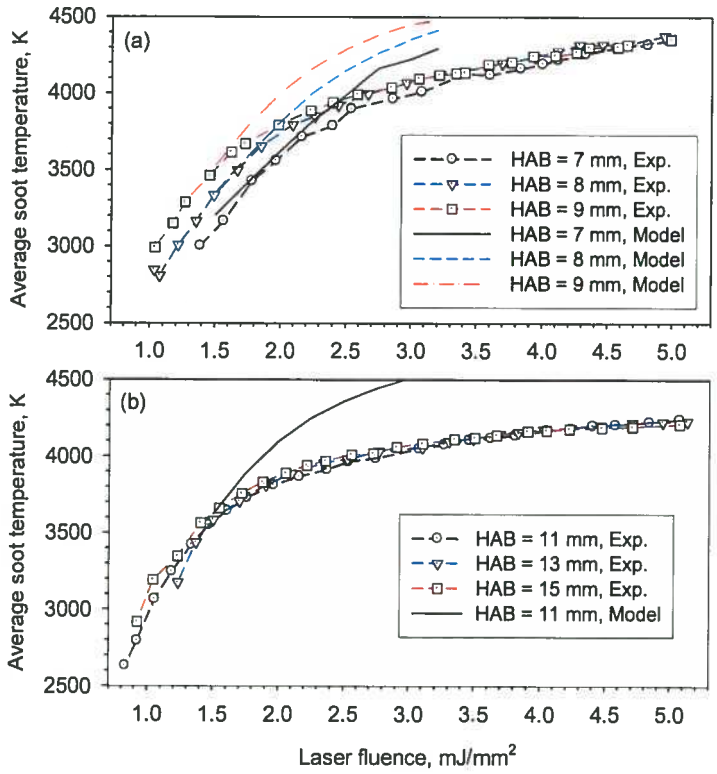

Fig. 17 Comparison of measured and modeled averaged soot temperature over 10 ns after the laser peak: Model 2.